Energy & Environmental Science

ROYAL SOCIETY OF CHEMISTRY

PAPER

View Article Online
View Journal | View Issue

Cite this: *Energy Environ. Sci.*, 2020, **13**, 3129

K^+ modulated K^+/vacancy disordered layered oxide for high-rate and high-capacity potassium-ion batteries†

Zhitong Xiao,‡[a] Jiashen Meng,‡[a] Fanjie Xia,[ab] Jinsong Wu, *[ab] Fang Liu,[ab] Xiao Zhang,[a] Linhan Xu, [c] Xinming Lin[a] and Liqiang Mai *[ad]

Received 20th May 2020,
Accepted 5th August 2020

DOI: 10.1039/d0ee01607a

rsc.li/ees

With high theoretical capacity and applicable operating voltage, layered transition metal oxides are potential cathodes for potassium-ion batteries (PIBs). However, a K^+/vacancy ordered structure in these oxides limits the K^+ transport kinetics and storage sites so that the PIBs still have poor rate performance and low achievable capacity. Here, to effectively resolve the problem, a K^+/vacancy disordered P3-type structure is designed and synthesized by simply modulating the K^+ contents in Mn/Ni-based layered oxides. The effect of the K^+ contents in a series of $K_xMn_{0.7}Ni_{0.3}O_2$ (x = 0.4–0.7) oxides has been systematically studied and it is found that while the K^+/vacancy ordered superstructure is stable at low K^+ content ($x < 0.6$), a complete K^+/vacancy disordered structure forms at high K^+ content ($x > 0.6$), evidenced by selected area electron diffraction and voltage plateaus in the charge/discharge curves. The K^+/vacancy disordered $K_{0.7}Mn_{0.7}Ni_{0.3}O_2$ exhibits much better rate performance and higher discharge capacity, compared to the K^+/vacancy ordered $K_{0.4}Mn_{0.7}Ni_{0.3}O_2$. Molecular dynamic simulations confirm that the K^+/vacancy disordered structure possesses interconnected continuous channels for K^+ diffusion and more active storage sites. This discovery sheds light on rational design of K^+/vacancy disordered layered oxide cathodes for next-generation high-performance PIBs.

Broader context

There are clear, economic and practical drivers to explore alternative charge carriers to lithium ions in charge storage devices, with potassium being the most promising. However, most of the currently developed potassium-ion batteries (PIBs) fall short of figures of merit against lithium–ion systems. In particular, there is an urgent need to develop high capacity cathode materials, which is currently the limit factor of full-cell batteries. In this respect, layered transition metal oxides are promising cathodes for PIBs. However, these current oxide cathodes typically suffer from poor rate performance and low achievable capacity originated from the K^+/vacancy ordered structures, in which K^+ diffusion barriers and K^+ storage obstacles are quite high. Therefore, breaking the K^+/vacancy ordering to form a K^+/vacancy disordered structure is of great significance to enhance the electrochemical properties of these layered oxides. In this contribution, we designed and synthesized a complete K^+/vacancy disordered structure by simply modulating the K^+ contents in Mn/Ni-based layered oxides for the first time. The K^+/vacancy disordered $K_{0.7}Mn_{0.7}Ni_{0.3}O_2$ with high K^+ content exhibits high discharge capacity, excellent rate performance and outstanding cycling stability. Our findings will open up a simple and effective route to design K^+/vacancy layered oxide cathode materials for practical applications of high-rate and capacity PIBs.

[a] *State Key Laboratory of Advanced Technology for Materials Synthesis and Processing, School of Materials Science and Engineering, Wuhan University of Technology, Luoshi Road 122, Wuhan, 430070, P. R. China. E-mail: mlq518@whut.edu.cn, wujs@whut.edu.cn*

[b] *Nanostructure Research Centre (NRC), Wuhan University of Technology, Luoshi Road 122, Wuhan, 430070, P. R. China*

[c] *Department of Physics, Collaborative Innovation Center for Optoelectronic Semiconductors and Efficient Devices, Jiujiang Research Institute, Xiamen University, Xiamen, 361005, P. R. China*

[d] *Foshan Xianhu Laboratory of the Advanced Energy Science and Technology Guangdong Laboratory, Xianhu Hydrogen Valley, Foshan, 528200, P. R. China*

† Electronic supplementary information (ESI) available. See DOI: 10.1039/d0ee01607a

‡ These authors contributed equally to this work.

Introduction

Potassium-ion batteries (PIBs) have attracted increasing attention as a potential next-generation energy storage system due to the high natural abundance of K reserves and low standard redox potential of K^+/K (−2.936 *vs.* E^0).[1–5] Compared to other secondary battery systems, only a few cathode materials for PIBs have been developed to date due to much more stringent de-intercalation/intercalation requirement caused by the large ionic radius of K^+ (1.33 Å).[6–12] Among various cathode materials, layered transition metal oxides (K_xTMO_2; TM = Mn, Co, Ni, Fe, V, Cr, *etc.*, and mixtures of them) have been

intensively investigated as one of the most promising families of cathodes due to their relatively high theoretical capacities, appropriate operating potential and facile synthetic chemistry.[13–18] However, sluggish K^+ transport kinetics and limited K^+ storage sites lead to low achievable capacity and inferior rate capability, which hinders their practical applications in PIBs.[19–22]

The aforementioned issues are essentially originated from the K^+/vacancy ordered structures of layered transition metal oxides.[19,23,24] Such ordered structures make those oxides exhibit distinct voltage plateaus in electrochemical curves and numerous redox peaks in cyclic voltammetry (CV) curves.[20,21,25] The K^+/vacancy ordering enlarges the partial K^+ site energy that leads to high K^+ diffusion barriers and K^+ storage obstacles, thus decreasing the K^+ diffusion coefficient and limiting the storage sites for K^+.[19–21,26] Therefore, breaking the K^+/vacancy ordering to form a K^+/vacancy disordered structure is of great significance to enhance the electrochemical properties of these layered oxides.

In general, there are three types of ordering in layered transition metal oxides: TM^{n+} charge ordering, transition metal ordering and K^+/vacancy ordering.[27–31] TM^{n+} charge disordering is mainly controlled by the redox potentials (Fermi level) of TM^{n+}.[27,32] Small difference in redox potentials is favorable for the formation of TM^{n+} charge ordering. Transition metal ordering is mainly caused by the difference of TM^{n+} ionic radius.[27,33] Large difference (radius ratio >15%) in ionic radius is favorable for the formation of the ordered arrangement. The formation of K^+/vacancy ordering is not only influenced by the K^+–K^+ electrostatic repulsion, but also coupled to TM^{n+} charge ordering.[27,32,34,35] The K^+–K^+ electrostatic repulsion depends on the K^+ content and distribution in the K layers of the layered transition metal oxides. Although the K^+/vacancy disordering is rarely investigated in the K^+-containing layered oxide materials, Na^+/vacancy disordered structures have been studied in the Na^+-contained layered oxide systems.[27,29,36] One efficient approach is the introduction of doped TM^{n+} with compatible ionic radius but quite different Fermi levels into layered transition metal oxides to suppress the TM^{n+} charge ordering, thus resulting in the Na^+/vacancy disordering. For example, Wang *et al.*[29] designed a Na^+/vacancy disordered Ti-doped Mn/Ni-based layered oxide ($Na_{2/3}Ni_{1/3}Mn_{1/3}Ti_{1/3}O_2$) with good rate performance and high achievable capacity. Due to the same valence, smaller ionic radius ratio and substantial different redox potentials, partial Ti substitution for Mn in Mn/Ni-based layered oxide effectively refrains charge ordering and breaks the coupling to Na^+/vacancy ordering. The other promising method is *via* selecting TM^{n+} with different Fermi levels and similar ionic radius. For instance, Wang *et al.*[27] chose Cr^{3+} and Ti^{4+} to design a $Na_{0.6}Cr_{0.6}Ti_{0.4}O_2$ layered oxide, which showed high achievable capacity and good rate performance. Disordered arrangement of Cr^{3+} and Ti^{4+} in the TM layers prevents TM^{n+} charge ordering and thus Na^+/vacancy ordering as well. In our work, different from the above-mentioned strategies, we found that strong K^+–K^+ electrostatic repulsion by increasing the K^+ content among the TM layers could induce a complete K^+/vacancy disordered structure. To the best of our knowledge, such a simple and effective strategy has never been developed previously for transforming a complex oxide from ordered to disordered structure, which has great potential to achieve high electrochemical performance in PIBs.

Herein, to explore the transformation from ordered to disordered structure and its impact on the electrochemical performance in PIBs, we employed Mn/Ni-based layered oxides ($K_xMn_{0.7}Ni_{0.3}O_2$) with a high redox potential and highly symmetric crystalline structures.[14,15,37,38] By investigating the impact of K^+ content to the layer configurations in $K_xMn_{0.7}Ni_{0.3}O_2$, it is found that with the increase of K^+ content from 0.4 to 0.7, a transition from K^+/vacancy ordering to disordering occurs. With increased K^+ being incorporated into the oxides, the interlayered K^+–K^+ electrostatic repulsion has been changed. Also the energy difference of the occupied K^+ sites has been reduced, which leads to breaking of the K^+/vacancy ordered structure. Moreover, a high K^+ content in the layered oxides can not only reduce the average oxidation state of the TM^{n+}, but also maintain more K^+ in the interlayers when the same amount of K^+ is extracted, which provides additional capacity and enhances the structural stability.[39] The obtained K^+/vacancy disordered P3-type $K_{0.7}Mn_{0.7}Ni_{0.3}O_2$ with high K^+ content as a cathode for PIBs exhibits high discharge capacity, excellent rate performance and outstanding cycling stability. Incorporated with various experimental measurements such as *in situ* X-ray diffraction characterization and molecular dynamic simulation calculations, the K^+ de-intercalation/intercalation mechanism was also investigated to reveal the intrinsic relationship between the K^+/vacancy disordered interlayer structure and K^+ transport kinetics.

Results and discussion

A series of characterizations were conducted to unveil the structure of $K_{0.4}Mn_{0.7}Ni_{0.3}O_2$ and $K_{0.7}Mn_{0.7}Ni_{0.3}O_2$ (Fig. 1). The X-ray diffraction (XRD) patterns and Rietveld refinement of $K_{0.4}Mn_{0.7}Ni_{0.3}O_2$ and $K_{0.7}Mn_{0.7}Ni_{0.3}O_2$ samples are shown in Fig. 1a and b, respectively. All diffraction peaks are identified as a P3-type layered structure, which belongs to a hexagonal symmetry.[40] The illustration of the P3-type crystalline structure is shown in the inset of Fig. 1a and b and Fig. S1 (ESI†). The O ions arrange the parallel layers for the ABBCCA sequence, with K^+ occupying the prismatic sites, and TM^{n+} (TM = Mn, Ni) sitting in the octahedral sites.[21,41] Comparing the structural information and lattice parameters of $K_{0.4}Mn_{0.7}Ni_{0.3}O_2$ ($a = b = 2.8858$ Å, $c = 20.8494$ Å) with those of $K_{0.7}Mn_{0.7}Ni_{0.3}O_2$ ($a = b = 2.8879$ Å, $c = 20.5893$ Å) (Tables S1 and S2, ESI†), increased K^+ content (from 0.4 to 0.7) leads to the expansion of the TM layers and the contraction of the K layers, which is attributed to the decrease of electrostatic repulsion between the O layers. This result is clearly shown in zoomed-in images of the XRD patterns for the (003) and (006) peaks in Fig. S2 (ESI†). Notably, the ordered structure in the $K_{0.4}Mn_{0.7}Ni_{0.3}O_2$ can be clearly identified by the superlattice spots (*e.g.* 1/3(110) and 1/3(1−20)) in the [−111] and [001] selected area electron

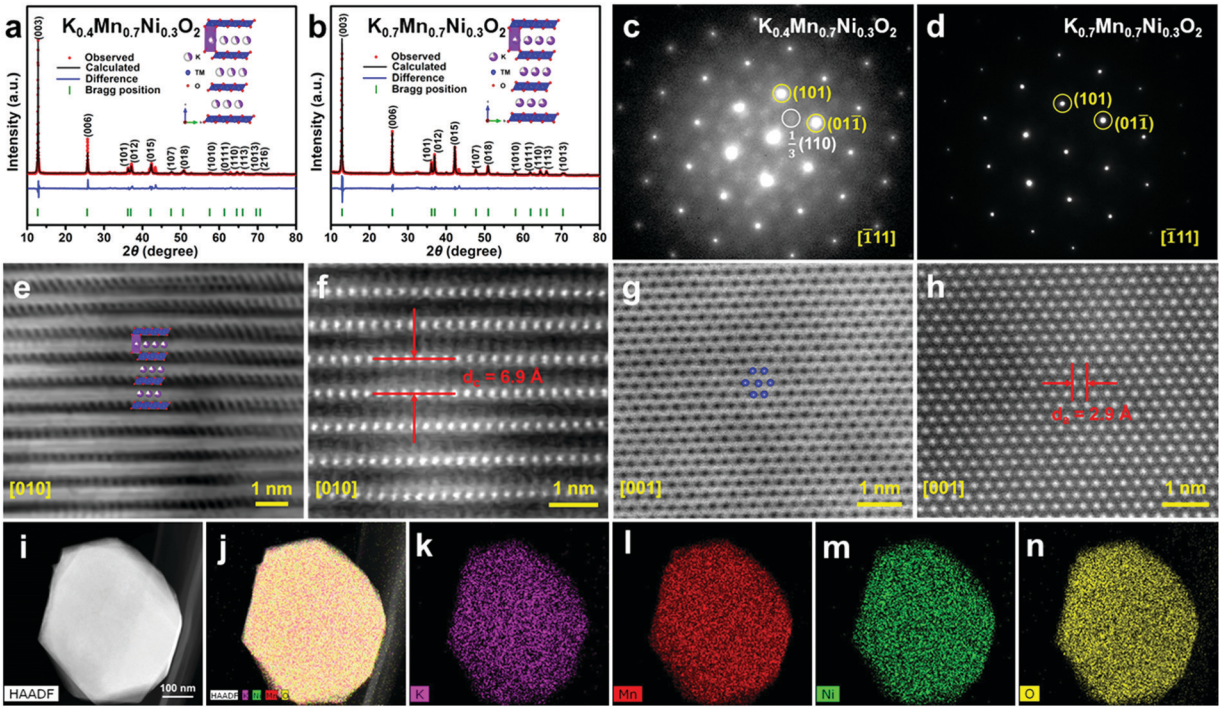

Fig. 1 Structural characterization of $K_{0.4}Mn_{0.7}Ni_{0.3}O_2$ and $K_{0.7}Mn_{0.7}Ni_{0.3}O_2$. XRD Rietveld refinement of $K_{0.4}Mn_{0.7}Ni_{0.3}O_2$ (a) and $K_{0.7}Mn_{0.7}Ni_{0.3}O_2$ (b) (inset: crystal structure viewed). SAED patterns along the [−111] zone axis of $K_{0.4}Mn_{0.7}Ni_{0.3}O_2$ (c) and $K_{0.7}Mn_{0.7}Ni_{0.3}O_2$ (d). ABF-STEM (e) and HAADF-STEM (f) images of $K_{0.7}Mn_{0.7}Ni_{0.3}O_2$ along the [010] zone axis. ABF-STEM (g) and HAADF-STEM (h) images of $K_{0.7}Mn_{0.7}Ni_{0.3}O_2$ along the [001] zone axis. (i–n) HAADF-STEM image of $K_{0.7}Mn_{0.7}Ni_{0.3}O_2$ and the corresponding EDS mappings for K, Mn, Ni, and O elements.

diffraction (SAED) pattern (Fig. 1c and Fig. S3, ESI†). In contrast, such superlattice spots do not exist in the [−111] SAED pattern of the $K_{0.7}Mn_{0.7}Ni_{0.3}O_2$, implying that this is a disordered structure (Fig. 1d). Such a K^+/vacancy ordering to disordering transition can also be confirmed as there are faint and additional peaks observed in the XRD pattern of $K_{0.4}Mn_{0.7}Ni_{0.3}O_2$ (Fig. S4, ESI†).[23] Detailed atomic-scale crystal structure information about $K_{0.7}Mn_{0.7}Ni_{0.3}O_2$ was acquired by aberration-corrected scanning transmission electron microscopy (STEM) with annular bright-field (ABF) and high-angle annular dark-field (HAADF) detectors. The O and K layers correspond to the points with slightly grey dotted contrast in the interlayer columns in the ABF-STEM images. Alternate K layers and TM layers coupled with O stack columns of ABBCCA can be clearly observed along the [010] zone axis in the ABF-STEM image, which is accordance with the atomic model of the P3-type structure (Fig. 1e). The HAADF-STEM image (Fig. 1f) exhibits that the measured distance of the adjacent layers is about 0.69 nm, which matches well with the interslab distance from XRD refinement data. The TM atoms arrange to form a hexagonal symmetry, which is observed in the ABF-STEM image along the [001] zone axis (Fig. 1g). The distance of 0.29 nm can be measured for the spacing of adjacent TM atoms in the HAADF-STEM images, corresponding to the XRD refinement cell parameter a (2.8879 Å) (Fig. 1h). The ABF-STEM and HAADF-STEM images along the [010] and [001] zone axis are also used to observe the detailed atomic-scale crystal structure information about $K_{0.4}Mn_{0.7}Ni_{0.3}O_2$, which corresponds to the XRD refinement results (Fig. S5, ESI†). From the scanning electron microscopy (SEM) and transmission electron microscopy (TEM) images (Fig. S6a, b, d, and e, ESI†), both $K_{0.4}Mn_{0.7}Ni_{0.3}O_2$ and $K_{0.7}Mn_{0.7}Ni_{0.3}O_2$ samples show the particles with an average size of approximately 1 μm in diameter. The high-resolution TEM (HRTEM) images exhibit that the interlayer distance is measured to be 0.243 nm, which agrees well with the (012) plane of the P3-type layered structure (Fig. S6c and f, ESI†). Finally, the homogeneous distribution of K, Mn, Ni, and O elements throughout the whole particles can be observed in the EDS mapping images (Fig. 1i–n and Fig. S6g–l, ESI†).

In order to reveal the effect of K^+ content on the layer configurations, the K^+ contents of 0.2, 0.3, 0.4, 0.5, 0.6, 0.7, 0.8, and 0.9 were chosen in the synthesis. At the same time, the atomic ratio of Mn and Ni contents is fixed at 0.7/0.3 in all of the samples, and the synthesized samples are $K_{0.2}Mn_{0.7}Ni_{0.3}O_2$, $K_{0.3}Mn_{0.7}Ni_{0.3}O_2$, $K_{0.4}Mn_{0.7}Ni_{0.3}O_2$, $K_{0.5}Mn_{0.7}Ni_{0.3}O_2$, $K_{0.6}Mn_{0.7}Ni_{0.3}O_2$, $K_{0.7}Mn_{0.7}Ni_{0.3}O_2$, $K_{0.8}Mn_{0.7}Ni_{0.3}O_2$, and $K_{0.9}Mn_{0.7}Ni_{0.3}O_2$. According to the inductively coupled plasma (ICP) results (Table S3, ESI†), the measured K : Mn : Ni ratios of all the synthesized samples are close to the nominal compositions. From XRD patterns, all samples show the layered structure as the main phase (Fig. S7, Fig. 1a and b, ESI†). However, some reflection peaks in the XRD patterns of $K_{0.2}Mn_{0.7}Ni_{0.3}O_2$ and $K_{0.3}Mn_{0.7}Ni_{0.3}O_2$ can be indexed to Ni_2MnO_4 (JCPDS No. 00-036-0083), while several impure peaks appeared in the XRD patterns of $K_{0.8}Mn_{0.7}Ni_{0.3}O_2$ and $K_{0.9}Mn_{0.7}Ni_{0.3}O_2$. This implies that only $K_{0.4}Mn_{0.7}Ni_{0.3}O_2$,

$K_{0.5}Mn_{0.7}Ni_{0.3}O_2$, $K_{0.6}Mn_{0.7}Ni_{0.3}O_2$, and $K_{0.7}Mn_{0.7}Ni_{0.3}O_2$ are successfully synthesized to be the pure P3-type layered structure. Due to very weak scattering ability, although the superlattice reflections in XRD of the ordered structure ($K_{0.4}Mn_{0.7}Ni_{0.3}O_2$) are quite faint, the ordered to disordered structure transformation (from $K_{0.4}Mn_{0.7}Ni_{0.3}O_2$ to $K_{0.7}Mn_{0.7}Ni_{0.3}O_2$) is clearly identified by the voltage plateaus in electrochemical measurement and redox peaks in the CV curves discussed below.

The CV tests of the $K_xMn_{0.7}Ni_{0.3}O_2$ in PIBs were firstly evaluated ranging from 2.0 to 3.9 V (*vs.* K^+/K). The $K_{0.4}Mn_{0.7}Ni_{0.3}O_2$ shows four pairs of redox peaks at 2.21/2.04, 2.57/2.42, 3.29/3.12, and 3.89/3.79 V, implying K^+/vacancy ordering in the K layers (Fig. S8a, ESI†). The voltage plateaus in the first three discharge/charge curves agree well with the redox couples in the CV curves (Fig. S8e, ESI†). When the K^+ content increases from 0.4 to 0.6, the redox peaks at 2.21/2.04 and 2.57/2.42 V are gradually weakened, and the peaks at 3.89/3.79 V disappeared (Fig. S8a–c, ESI†). Meanwhile, the peaks at 3.29/3.12 V gradually shift towards high voltage (3.69/3.41 V for $K_{0.6}Mn_{0.7}Ni_{0.3}O_2$) and become obvious. The change of the corresponding voltage plateaus shows the same trend in their charge/discharge curves (Fig. S8e–g, ESI†). While the three redox couples of $K_{0.7}Mn_{0.7}Ni_{0.3}O_2$ disappeared, only one redox peak at 3.83/3.46 V remains (Fig. S8d, ESI†). Similarly, the typical charge/discharge curves of $K_{0.7}Mn_{0.7}Ni_{0.3}O_2$ become sloping within a large range of voltage upon K^+ extraction and insertion (Fig. S8h, ESI†). In addition, the charge/discharge curves of $K_{0.2}Mn_{0.7}Ni_{0.3}O_2$, $K_{0.3}Mn_{0.7}Ni_{0.3}O_2$, $K_{0.8}Mn_{0.7}Ni_{0.3}O_2$, and $K_{0.9}Mn_{0.7}Ni_{0.3}O_2$ are presented in Fig. S9 (ESI†). In general, the K^+/vacancy ordered layered transition metal oxides show numerous redox couples in the CV curves and distinct voltage plateaus in the electrochemical curves. Meanwhile, the smooth charge/discharge curves and small amount of redox couples in the CV curves can be observed in the K^+/vacancy disordered layered transition metal oxides. Therefore, these results indicated that the layer configurations of $K_xMn_{0.7}Ni_{0.3}O_2$ transform from K^+/vacancy ordering to K^+/vacancy disordering when the K^+ content increases from 0.4 to 0.7.

To identify their structure–property relationships, the electrochemical performances were investigated by electrochemical measurements as the PIB cathode in 2.0–3.9 V (*vs.* K^+/K) (Fig. 2).

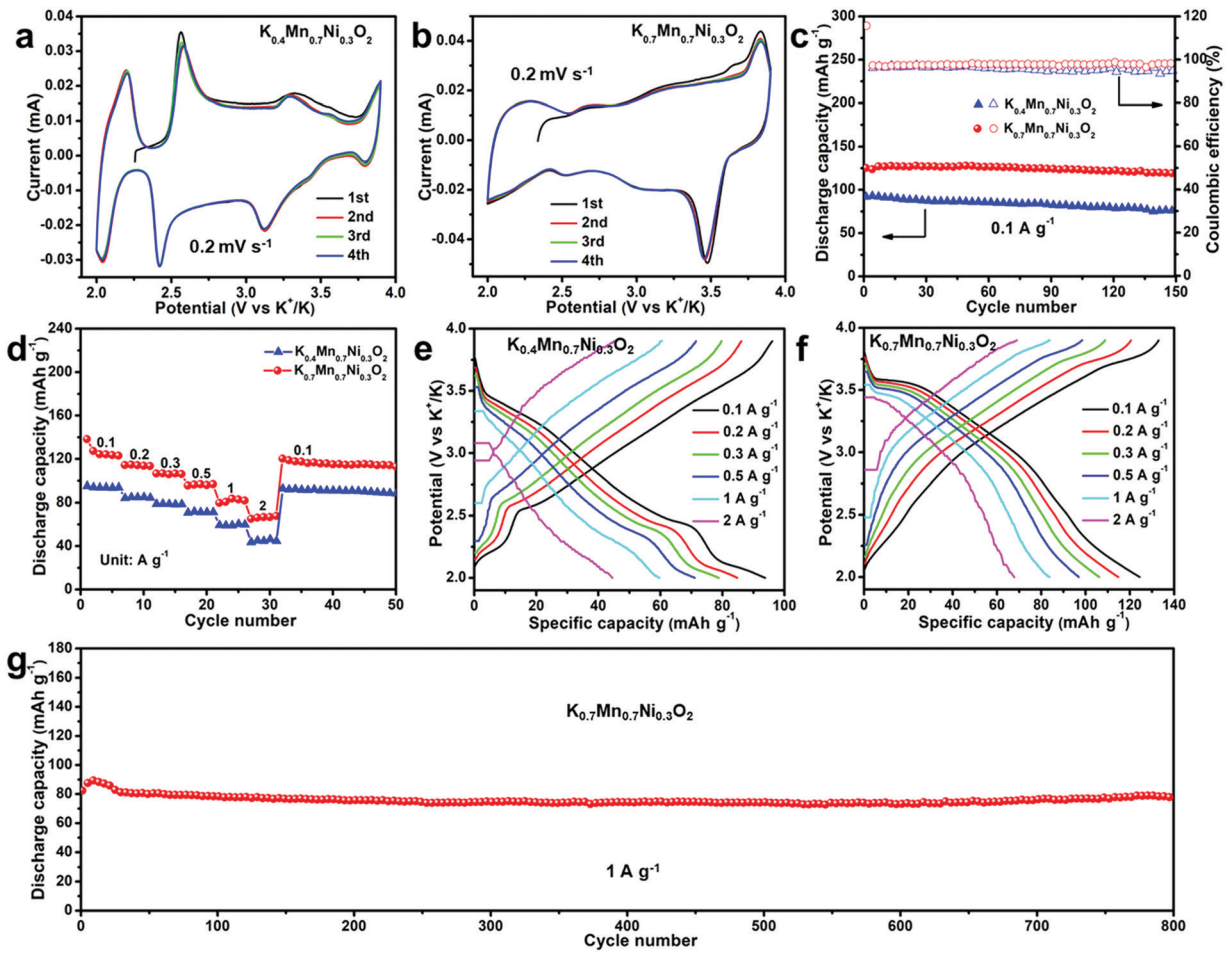

Fig. 2 Electrochemical performances of $K_{0.4}Mn_{0.7}Ni_{0.3}O_2$ and $K_{0.7}Mn_{0.7}Ni_{0.3}O_2$ in 2.0–3.9 V (*vs.* K^+/K). CV curves of the first four cycles at 0.2 mV s^{-1} of $K_{0.4}Mn_{0.7}Ni_{0.3}O_2$ (a) and $K_{0.7}Mn_{0.7}Ni_{0.3}O_2$ (b). (c) Cycling performance with Coulombic efficiencies measured at 0.1 A g^{-1}. (d) Rate performance conducted at 0.1, 0.2, 0.3, 0.5, 1, 2, and back to 0.1 A g^{-1}. The corresponding discharge/charge curves of $K_{0.4}Mn_{0.7}Ni_{0.3}O_2$ (e) and $K_{0.7}Mn_{0.7}Ni_{0.3}O_2$ (f) at different rates. (g) Long-term cyclic performance of $K_{0.7}Mn_{0.7}Ni_{0.3}O_2$ at 1 A g^{-1}.

Four pairs of redox peaks are observed in the CV curves of $K_{0.4}Mn_{0.7}Ni_{0.3}O_2$ (Fig. 2a). One couple at 3.89/3.79 V can be related to the redox reactions of nickel element. Another three pairs of redox peaks at 2.21/2.04, 2.57/2.42 and 3.29/3.12 V can originate from the rearrangement of the K^+/vacancy ordered structure in the K layer during K^+ de-intercalation/intercalation.[14] In contrast, CV curves of $K_{0.7}Mn_{0.7}Ni_{0.3}O_2$ show only one pair of redox peaks at 3.83/3.46 V, which is also attributed to the redox reactions of nickel element (Fig. 2b). This indicates the formation of K^+/vacancy disordered structure when the K^+ content varies from 0.4 to 0.7.[29] The $K_{0.7}Mn_{0.7}Ni_{0.3}O_2$ electrode shows a higher discharge specific capacity of 125.4 mA h g^{-1} and higher average discharge voltage of 3.0 V than those of $K_{0.4}Mn_{0.7}Ni_{0.3}O_2$ (93.9 mA h g^{-1} and 2.7 V) when testing at 0.1 A g^{-1} (Fig. 2c and Fig. S10, ESI†). After 150 cycles, striking capacity retention of 93.6% could be obtained for $K_{0.7}Mn_{0.7}Ni_{0.3}O_2$ compared with 81.3% for $K_{0.4}Mn_{0.7}Ni_{0.3}O_2$. Surprisingly, as compared in the rate performance in Fig. 2d, higher average discharge capacities of 124.2, 114.2, 106.6, 96.9, 83.8, and 67.8 mA h g^{-1} for $K_{0.7}Mn_{0.7}Ni_{0.3}O_2$ are obtained at 0.1, 0.2, 0.3, 0.5, 1, and 2 A g^{-1}, respectively. Meanwhile, the $K_{0.4}Mn_{0.7}Ni_{0.3}O_2$ electrode shows the corresponding capacities of 93.7, 84.8, 78.6, 71.1, 58.9, and 44.5 mA h g^{-1}, respectively. The corresponding discharge/charge curves of rate performance imply ultrafast K^+ storage and low polarization of the K^+/vacancy disordered $K_{0.7}Mn_{0.7}Ni_{0.3}O_2$ (Fig. 2e and f). In particular, the $K_{0.7}Mn_{0.7}Ni_{0.3}O_2$ electrode also exhibits superior long-term cyclic stability with a retained capacity of 78.8 mA h g^{-1} even after 800 cycles at 1 A g^{-1} (capacity retention of 88.5%, corresponding to an average capacity loss of 0.014% per cycle) (Fig. 2g). By comparison, the $K_{0.4}Mn_{0.7}Ni_{0.3}O_2$ electrode shows fast capacity decay from 56.2 mA h g^{-1} to 34.6 mA h g^{-1} after 800 cycles, corresponding to 61.6% capacity retention (Fig. S11, ESI†). Therefore, $K_{0.7}Mn_{0.7}Ni_{0.3}O_2$ displayed fast K^+ storage and superior long-term cycling stability, which is mainly attributed to the K^+/vacancy disordered interlayer structure. In addition, the cycling performances of $K_{0.7}Mn_{0.7}Ni_{0.3}O_2$ at 0.2 and 0.5 A g^{-1} were measured (Fig. S12, ESI†). After 200 and 500 cycles, high capacity retentions of 90.2% and 86.2% were achieved, respectively, confirming its long-term cycling stability closed to the typical battery operating conditions. Furthermore, the electrochemical performance of $K_{0.7}Mn_{0.7}Ni_{0.3}O_2$ at high mass loadings was investigated (Fig. S13, ESI†). When tested at 0.2 A g^{-1} after 200 cycles, $K_{0.7}Mn_{0.7}Ni_{0.3}O_2$ possesses a high reversible capacity of 85.5 mA h g^{-1} and a high capacity retention of 85.7% a high mass loading of 9.38 mg cm^{-2} (Fig. S13a, ESI†). $K_{0.7}Mn_{0.7}Ni_{0.3}O_2$ also exhibits excellent rate performance with a high mass loading of 9.56 mg cm^{-2}. Highly reversible average discharge capacities of 103.6, 96.0, 90.5, 81.3, 67.9, and 54.6 mA h g^{-1} are obtained at 0.1, 0.2, 0.3, 0.5, 1, and 2 A g^{-1}, respectively (Fig. S13b, ESI†). Therefore, the achieved high areal capacity ($\sim$1.0 mA h cm^{-2}) with stable cycling properties and good rate performance demonstrated that the $K_{0.7}Mn_{0.7}Ni_{0.3}O_2$ is a promising cathode candidate for PIBs. The SEM and TEM images after cycling for $K_{0.4}Mn_{0.7}Ni_{0.3}O_2$ and $K_{0.7}Mn_{0.7}Ni_{0.3}O_2$ are presented in Fig. S14 (ESI†). Compared with previously reported layered oxide cathodes, the K^+/vacancy disordered $K_{0.7}Mn_{0.7}Ni_{0.3}O_2$ also manifested great competitiveness for superior electrochemical performances in PIBs (Table S4, ESI†).

X-ray photoelectron spectroscopy (XPS) measurement was carried out to explore the electrochemical mechanism during the K^+ de-intercalation/intercalation processes (Fig. S15 and S16, ESI†). For $K_{0.7}Mn_{0.7}Ni_{0.3}O_2$, the observed binding energies are consistent with Mn^{4+} and Ni^{2+}.[42] The binding energies of Ni $2p_{1/2}$ and Ni $2p_{3/2}$ in $K_{0.4}Mn_{0.7}Ni_{0.3}O_2$ are higher than those in $K_{0.7}Mn_{0.7}Ni_{0.3}O_2$, and the binding energies of Mn $2p_{1/2}$ and Mn $2p_{3/2}$ are similar for $K_{0.4}Mn_{0.7}Ni_{0.3}O_2$ and $K_{0.7}Mn_{0.7}Ni_{0.3}O_2$ (Fig. S15b and c, ESI†). These results indicate that the valence of Ni in $K_{0.4}Mn_{0.7}Ni_{0.3}O_2$ is higher than divalent, and Mn is tetravalent.[29,42] During the charge/discharge process, no apparent shift for the Mn 2p spectra of $K_{0.7}Mn_{0.7}Ni_{0.3}O_2$ is observed, indicating that the Mn^{4+} is electrochemically inactive (Fig. S16a, ESI†). The peaks of Ni $2p_{1/2}$ and Ni $2p_{3/2}$ shift to higher binding energy during the K^+ de-intercalation process, demonstrating the oxidation of Ni^{2+} (Fig. S16b, ESI†). Following discharge to 2.0 V, the peaks shift toward lower binding energy, suggesting the reduction process of Ni. A similar phenomenon could be observed for $K_{0.4}Mn_{0.7}Ni_{0.3}O_2$ as shown in Fig. S16c and d (ESI†), implying that the electrochemically active Ni^{2+} provides charge compensation, and the Mn^{4+} serves as a stabilizer in the K–Mn–Ni–O system.

The crystalline structure evolutions of $K_{0.4}Mn_{0.7}Ni_{0.3}O_2$ and $K_{0.7}Mn_{0.7}Ni_{0.3}O_2$ were monitored using *in situ* XRD measurements to unveil the K^+ de-intercalation/intercalation mechanism (Fig. 3 and Fig. S17, ESI†). When changing from open-circuit voltage (or 2.0 V) to 3.75 V, the (006) peak of $K_{0.7}Mn_{0.7}Ni_{0.3}O_2$ gradually shifts toward low angle, whereas the (101), (012) and (015) peaks shift to high angle. These phenomena are attributed to the expansion of the *c* axis and the constriction of the *a*–*b* plane, which are caused by the increased electrostatic repulsion between the O layers when K^+ is extracted. The peak intensities of the (101), (012) and (015) planes were weakened but did not disappear, and a new diffraction peak appeared at 40.5° after being charged continually to 3.9 V and then discharged to 3.5 V (green marker in Fig. S17d–f, ESI†). The new peak can be indexed to the (104) of the O3 phase, corresponding to the phase transformation between P3 and O3 for $K_{0.7}Mn_{0.7}Ni_{0.3}O_2$ at high potential.[43] As K^+ is being inserted (down to 2.0 V), the (006) peak re-shifts towards high angle, and the (101), (012) and (015) peaks re-shift to low angle. At this stage, electrostatic repulsion between the oxygen layers is decreased when K^+ is inserted into the interlayers. The shift behaviour for the first two cycles is similar and all the peaks could return to the initial state of pure P3 phase, demonstrating the highly reversible K^+ de-intercalation/intercalation process, and thus high cycling stability of $K_{0.7}Mn_{0.7}Ni_{0.3}O_2$. Notably, although the structure evolution of $K_{0.4}Mn_{0.7}Ni_{0.3}O_2$ is similar to that of $K_{0.7}Mn_{0.7}Ni_{0.3}O_2$, there are three main differences: (1) the shift behaviour of the (101), (012) and (015) peaks of $K_{0.4}Mn_{0.7}Ni_{0.3}O_2$ is more complicated when discharging from 2.5 V to 2.0 V and then charging to 2.7 V. They shift to high angle and then towards low angle, and repeat this process during the charging range (within the blue

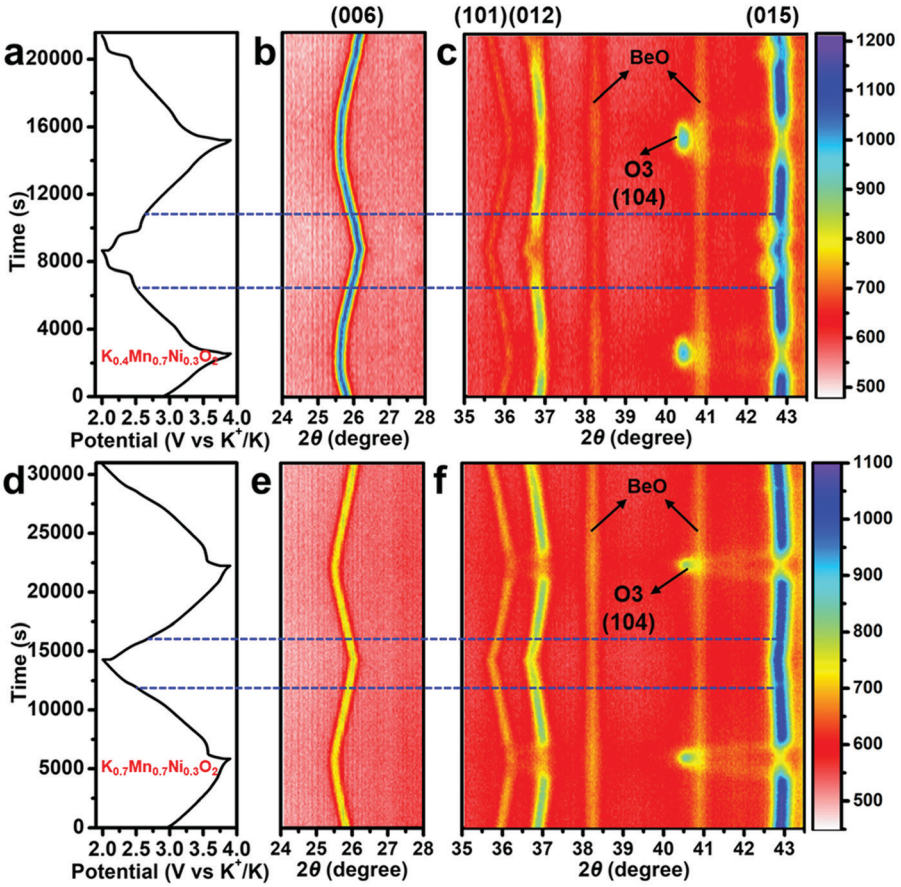

Fig. 3 *In situ* XRD characterization of $K_{0.4}Mn_{0.7}Ni_{0.3}O_2$ and $K_{0.7}Mn_{0.7}Ni_{0.3}O_2$. Discharge/charge curves during the first two cycles at 0.05 A g^{-1} in 2.0–3.9 V of $K_{0.4}Mn_{0.7}Ni_{0.3}O_2$ (a) and $K_{0.7}Mn_{0.7}Ni_{0.3}O_2$ (d). (b and c) Two-dimensional *in situ* XRD patterns at 24–28° and 35–43.5° of $K_{0.4}Mn_{0.7}Ni_{0.3}O_2$. (e and f) Two-dimensional *in situ* XRD patterns at 24–28° and 35–43.5° of $K_{0.7}Mn_{0.7}Ni_{0.3}O_2$.

dotted line in Fig. 3a–c). (2) The peak intensities of the (101), (012) and (015) planes of $K_{0.4}Mn_{0.7}Ni_{0.3}O_2$ are obviously weakened during the above-mentioned process. (3) In contrast with $K_{0.4}Mn_{0.7}Ni_{0.3}O_2$, all the lattice parameters of *a*, *c* and cell volume of $K_{0.7}Mn_{0.7}Ni_{0.3}O_2$ vary along with the slope of the electrochemical curves (Fig. S18, ESI†). These phenomena are all caused by the rearrangement of different interlayer K^+/vacancy orderings for $K_{0.4}Mn_{0.7}Ni_{0.3}O_2$, corresponding to the voltage plateaus in the electrochemical curves. In addition, the K^+/vacancy disordered structure of $K_{0.7}Mn_{0.7}Ni_{0.3}O_2$ remains during the charge and discharge process, which was proved by the XRD and SAED patterns at the charged state (Fig. S19, ESI†).

To verify the advantages of K^+/vacancy disordering on diffusion kinetics, the diffusion coefficients of K^+ of $K_{0.4}Mn_{0.7}Ni_{0.3}O_2$ and $K_{0.7}Mn_{0.7}Ni_{0.3}O_2$ are revealed by the galvanostatic intermittent titration technique (GITT) (Fig. S20, ESI†). The theoretical initial charge and discharge specific capacities of $K_{0.7}Mn_{0.7}Ni_{0.3}O_2$ are 113 and 129.6 mA h g^{-1}, respectively, corresponding to 0.49 mol K^+ extraction and 0.56 mol K^+ insertion per unit formula (Fig. S20a, ESI†). And the corresponding values of $K_{0.4}Mn_{0.7}Ni_{0.3}O_2$ are 72.5 (0.28 mol) and 98.6 mA h g^{-1} (0.38 mol), respectively (Fig. S20b, ESI†). The K^+ diffusion coefficients of $K_{0.7}Mn_{0.7}Ni_{0.3}O_2$ are calculated to be 10^{-11} to 10^{-10} cm^2 s^{-1}, one order of magnitude higher than those of $K_{0.4}Mn_{0.7}Ni_{0.3}O_2$ (10^{-12} to 10^{-11} cm^2 s^{-1}) (Fig. S20c, ESI†). In addition, the K^+ diffusion coefficient values show no jumps for $K_{0.7}Mn_{0.7}Ni_{0.3}O_2$, which agrees well with the smooth characteristic of the charge/discharge curves, a character attributed to K^+/vacancy disordering. The electrochemical impedance spectroscopy (EIS) plots show a lower charge transfer resistance and faster K^+ transport kinetics of $K_{0.7}Mn_{0.7}Ni_{0.3}O_2$ than those of $K_{0.4}Mn_{0.7}Ni_{0.3}O_2$, suggesting faster electronic and ion transport for a K^+/vacancy disordered structure (Fig. S21, ESI†).

Molecular dynamic simulation calculations were also performed to calculate K^+ transport properties in the K^+/vacancy disordered $K_{0.7}Mn_{0.7}Ni_{0.3}O_2$ and K^+/vacancy ordered $K_{0.4}Mn_{0.7}Ni_{0.3}O_2$, respectively, as shown in Fig. 4a and c. Two-dimension diffusion paths are confirmed for the K^+ migration in the K layer of the crystal structure. The corresponding top views of the K^+ migration trajectories in a single K layer show that the K^+ transport trajectory of $K_{0.7}Mn_{0.7}Ni_{0.3}O_2$ is more interconnected and homogeneous than that of $K_{0.4}Mn_{0.7}Ni_{0.3}O_2$. This result suggests that K^+/vacancy disordering provides interconnected and continuous channels for the K^+ transport and reduces the energy difference of K^+ sites, which endows $K_{0.7}Mn_{0.7}Ni_{0.3}O_2$ with fast K^+ transport kinetics and more K^+ storage sites.

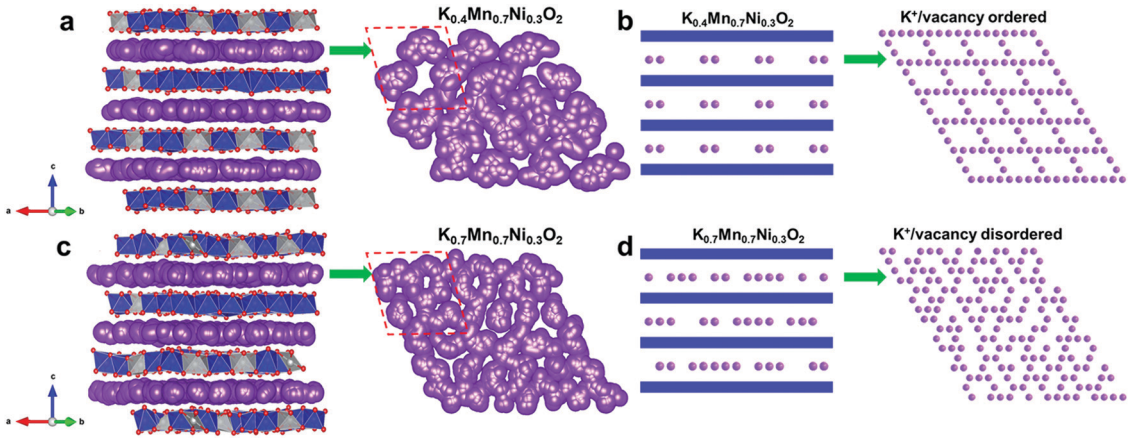

Fig. 4 Molecular dynamic simulation calculations and K^+/vacancy structure illustration of $K_{0.4}Mn_{0.7}Ni_{0.3}O_2$ and $K_{0.7}Mn_{0.7}Ni_{0.3}O_2$. Trajectories simulation of K^+ in $K_{0.4}Mn_{0.7}Ni_{0.3}O_2$ (a) and $K_{0.7}Mn_{0.7}Ni_{0.3}O_2$ (c), the right panel figure is the top view of each K^+ layer. K^+/vacancy structure illustrations of $K_{0.4}Mn_{0.7}Ni_{0.3}O_2$ (b) and $K_{0.7}Mn_{0.7}Ni_{0.3}O_2$ (d). The purple balls represent K^+.

On the basis of the structure characterization, electrochemical measurement, electrochemical mechanism and K^+ transport kinetics analysis, the K^+/vacancy structure of $K_{0.4}Mn_{0.7}Ni_{0.3}O_2$ and $K_{0.7}Mn_{0.7}Ni_{0.3}O_2$ can be illustrated as shown in Fig. 4b and d. For $K_{0.4}Mn_{0.7}Ni_{0.3}O_2$, the distribution of K^+ and vacancies exhibits an obvious periodicity and their positions are fixed, which forms the K^+/vacancy ordered structure (Fig. 4b). In contrast, the location and arrangement of K^+ and vacancies in $K_{0.7}Mn_{0.7}Ni_{0.3}O_2$ are random, suggesting the K^+/vacancy disordered structure (Fig. 4d).

To demonstrate its practical application, the K-ion full battery has been fabricated using soft carbon as an anode and $K_{0.7}Mn_{0.7}Ni_{0.3}O_2$ as a cathode (Fig. 5). The XRD pattern, SEM image, Raman spectrum, and electrochemical performances of soft carbon are presented in Fig. S22 (ESI†). Before full cell assembly, the soft carbon anode was pre-cycled at 0.01 to 1.50 V (*vs.* K^+/K) to form the stable solid–electrolyte interphase (SEI) layer and activate the electrode material for 20 cycles. The capacity ratio between the anode and cathode is adjusted to be 1.2 to eliminate the irreversibility. The charge–discharge voltage profiles at 0.1 A g^{-1} in 1.1–3.5 V exhibit that the initial charge and discharge specific capacities are 87.5 and 95.1 mA h g^{-1} (based on the mass of the cathode), respectively (Fig. 5a). A slightly increased discharging capacity in cycling is ascribed as the pre-potassiation process of the soft carbon anode before fabricating the full battery. The reversible discharge capacity reaches 82.2 mA h g^{-1} after 100 cycles, which equals to 86.4% of the initial discharge capacity (Fig. 5b). The full cell delivers a considerable rate performance with the discharge capacity of 92.6, 85.9, 80.0, 73.4, and 65.3 mA h g^{-1} at 0.1, 0.2, 0.3, 0.4,

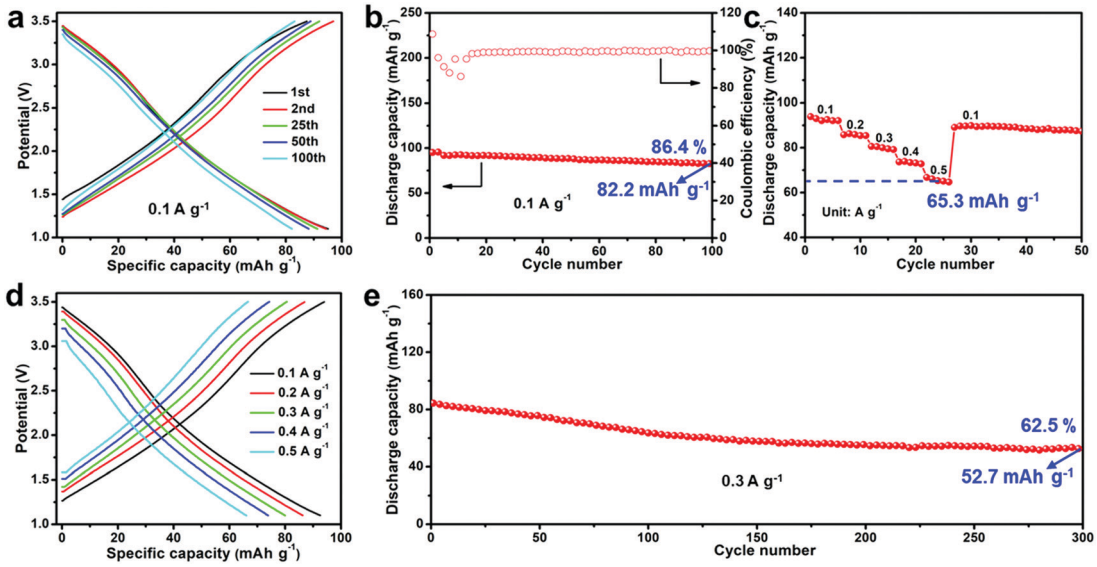

Fig. 5 Electrochemical performance of the K-ion full battery based on $K_{0.7}Mn_{0.7}Ni_{0.3}O_2$/soft carbon in 1.1–3.5 V. (a) Charge/discharge curves at 0.1 A g^{-1}. (b) Cycling performance and the corresponding Coulombic efficiencies tested at 0.1 A g^{-1}. Rate performance (c) conducted at 0.1, 0.2, 0.3, 0.4, and 0.5 A g^{-1} and the corresponding discharge/charge curves at different rates (d). (e) Long-term cycling capability at 0.3 A g^{-1}.

and 0.5 A g^{-1}, respectively (Fig. 5c and d). When tested at 0.3 A g^{-1}, the full cell also exhibits good cycling stability with 62.5% capacity retention after 300 cycles (Fig. 5e), showing great potential in commercial applications.

Conclusions

By simply modulating the K^+ contents in a series of $K_xMn_{0.7}Ni_{0.3}O_2$ layered oxides, an ordered-to-disordered structural change has been identified. The interlayered structure configurations of $K_xMn_{0.7}Ni_{0.3}O_2$ evolve from a K^+/vacancy ordered structure to a K^+/vacancy disordered structure when the K^+ content increases from 0.4 to 0.7. The high K^+ content affects interlayered K^+–K^+ electrostatic repulsion and reduces the energy difference of the K^+ sites, thus breaking the K^+/vacancy ordered structure. As a result, the K^+/vacancy disordered P3-type $K_{0.7}Mn_{0.7}Ni_{0.3}O_2$ as a PIB cathode exhibits outstanding rate capability (67.8 mA h g^{-1} at 2 A g^{-1}) and high discharge capacity (125.4 mA h g^{-1} at 0.1 A g^{-1}). The enhanced electrochemical performance is attributed to the fast K^+ transport kinetics ($\sim 10^{-11}$ cm^2 s^{-1}) and more reversible active K^+ storage sites provided by the K^+/vacancy disordered structure. Moreover, the $K_{0.7}Mn_{0.7}Ni_{0.3}O_2$ also exhibits excellent rate performance and cycling stability when used as a cathode in K-ion full batteries. Our discovery opens a simple and effective route to design K^+/vacancy layered oxide cathode materials for practical application of high-rate and capacity PIBs.

Conflicts of interest

There are no conflicts to declare.

Acknowledgements

This work was supported by the National Natural Science Foundation of China (51832004, 51521001), the National Key Research and Development Program of China (2016YFA0202603), the Programme of Introducing Talents of Discipline to Universities (B17034), the Natural Science Foundation of Hubei Province (2019CFA001), and the Foshan Xianhu Laboratory of the Advanced Energy Science and Technology Guangdong Laboratory (XHT2020-003). The S/TEM work was performed at the Nanostructure Research Center (NRC), which is supported by the Fundamental Research Funds for the Central Universities (WUT: 2019III012GX, 2020III002GX), the State Key Laboratory of Advanced Technology for Materials Synthesis and Processing.

Notes and references

1 W. Zhang, Y. Liu and Z. Guo, *Sci. Adv.*, 2019, **5**, eaav7412.
2 Q. Zhang, Z. Wang, S. Zhang, T. Zhou, J. Mao and Z. Guo, *Electrochem. Energy Rev.*, 2018, **1**, 625–658.
3 H. Kim, J. C. Kim, M. Bianchini, D.-H. Seo, J. Rodriguez-Garcia and G. Ceder, *Adv. Energy Mater.*, 2018, **8**, 1702384.
4 X. Wu, D. P. Leonard and X. Ji, *Chem. Mater.*, 2017, **29**, 5031–5042.
5 R. Rajagopalan, Y. Tang, X. Ji, C. Jia and H. Wang, *Adv. Funct. Mater.*, 2020, **30**, 1909486.
6 H. Wang, D. Yu, X. Wang, Z. Niu, M. Chen, L. Cheng, W. Zhou and L. Guo, *Angew. Chem., Int. Ed.*, 2019, **58**, 16451–16455.
7 A. S. Hameed, A. Katogi, K. Kubota and S. Komaba, *Adv. Energy Mater.*, 2019, **9**, 1902528.
8 X. Wang, Y. Li, S. Wang, F. Zhou, P. Das, C. Sun, S. Zheng and Z. S. Wu, *Adv. Energy Mater.*, 2020, **10**, 2000081.
9 Y. Dong, H. Shi and Z. S. Wu, *Adv. Funct. Mater.*, 2020, **30**, 2000706.
10 W. B. Park, S. C. Han, C. Park, S. U. Hong, U. Han, S. P. Singh, Y. H. Jung, D. Ahn, K.-S. Sohn and M. Pyo, *Adv. Energy Mater.*, 2018, **8**, 1703099.
11 J. Huang, X. Lin, H. Tan and B. Zhang, *Adv. Energy Mater.*, 2018, **8**, 1703496.
12 H. Lin, M. Li, X. Yang, D. Yu, Y. Zeng, C. Wang, G. Chen and F. Du, *Adv. Energy Mater.*, 2019, **9**, 1900323.
13 T. Deng, X. Fan, J. Chen, L. Chen, C. Luo, X. Zhou, J. Yang, S. Zheng and C. Wang, *Adv. Funct. Mater.*, 2018, **28**, 1800219.
14 X. Zhang, Y. Yang, X. Qu, Z. Wei, G. Sun, K. Zheng, H. Yu and F. Du, *Adv. Funct. Mater.*, 2019, **29**, 1905679.
15 J. H. Jo, J. U. Choi, Y. J. Park, Y. H. Jung, D. Ahn, T. Y. Jeon, H. Kim, J. Kim and S. T. Myung, *Adv. Energy Mater.*, 2020, **10**, 1903605.
16 J.-Y. Hwang, J. Kim, T.-Y. Yu, S.-T. Myung and Y.-K. Sun, *Energy Environ. Sci.*, 2018, **11**, 2821–2827.
17 T. Masese, K. Yoshii, Y. Yamaguchi, T. Okumura, Z. D. Huang, M. Kato, K. Kubota, J. Furutani, Y. Orikasa, H. Senoh, H. Sakaebe and M. Shikano, *Nat. Commun.*, 2018, **9**, 3823.
18 X. Wang, X. Xu, C. Niu, J. Meng, M. Huang, X. Liu, Z. Liu and L. Mai, *Nano Lett.*, 2017, **17**, 544–550.
19 H. Kim, J. C. Kim, S.-H. Bo, T. Shi, D.-H. Kwon and G. Ceder, *Adv. Energy Mater.*, 2017, **7**, 1700098.
20 T. Deng, X. Fan, C. Luo, J. Chen, L. Chen, S. Hou, N. Eidson, X. Zhou and C. Wang, *Nano Lett.*, 2018, **18**, 1522–1529.
21 H. Kim, D. H. Seo, J. C. Kim, S. H. Bo, L. Liu, T. Shi and G. Ceder, *Adv. Mater.*, 2017, **29**, 1702480.
22 K. Haegyeom, S. Dong-Hwa, U. Alexander, L. Jinhyuk, K. Deok-Hwang, B. Shou-Hang, S. Tan, J. K. Papp, B. D. McCloskey and C. Gerbrand, *Chem. Mater.*, 2018, **30**, 6532–6539.
23 M. Blangero, R. Decourt, D. Carlierlarregaray, G. Ceder, M. Pollet, J. P. Doumerc, J. Darriet and C. Delmas, *Inorg. Chem.*, 2010, **44**, 9299–9304.
24 M. Y. Toriyama, J. L. Kaufman and A. V. D. Ven, *ACS Appl. Energy Mater.*, 2019, **2**, 2629–2632.
25 S. Zhao, K. Yan, P. Munroe, B. Sun and G. Wang, *Adv. Energy Mater.*, 2019, **9**, 1803757.
26 G. J. Shu and F. C. Chou, *Phys. Rev. B: Condens. Matter Mater. Phys.*, 2008, **78**, 052101.
27 Y. Wang, R. Xiao, Y. S. Hu, M. Avdeev and L. Chen, *Nat. Commun.*, 2015, **6**, 6954.
28 R. Berthelot, D. Carlier and C. Delmas, *Nat. Mater.*, 2011, **10**, 74–80.

29 P.-F. Wang, H.-R. Yao, X.-Y. Liu, Y.-X. Yin, J.-N. Zhang, Y. Wen, X. Yu, L. Gu and Y.-G. Guo, *Sci. Adv.*, 2018, **4**, eaar6018.
30 X. Li, X. Ma, D. Su, L. Liu, R. Chisnell, S. P. Ong, H. Chen, A. Toumar, J. C. Idrobo and Y. Lei, *Nat. Mater.*, 2014, **13**, 586–592.
31 I. Dai, Y. Miyazaki, T. Kajitani and K. Yubuta, *Phys. Rev. B: Condens. Matter Mater. Phys.*, 2008, **78**, 184112.
32 Y. S. Meng, A. V. D. Ven, M. K. Y. Chan and G. Ceder, *Phys. Rev. B: Condens. Matter Mater. Phys.*, 2005, **72**, 2103.
33 Z. Chen, B. Radhakrishnan, I. H. Chu, Z. Wang and S. P. Ong, *Phys. Rev. Appl.*, 2017, **7**, 064003.
34 Y. S. Meng, Y. Hinuma and G. Ceder, *J. Chem. Phys.*, 2008, **128**, 12685.
35 G. J. Shu, A. Prodi, S. Y. Chu, Y. S. Lee, H. S. Sheu and F. C. Chou, *Phys. Rev. B: Condens. Matter Mater. Phys.*, 2007, **76**, 184115.
36 J. Vinckevičiūtė, M. D. Radin and A. Van der Ven, *Chem. Mater.*, 2016, **28**, 8640–8650.
37 C. Ma, J. Alvarado, J. Xu, R. J. Clement, M. Kodur, W. Tong, C. P. Grey and Y. S. Meng, *J. Am. Chem. Soc.*, 2017, **139**, 4835–4845.
38 P. F. Wang, Y. You, Y. X. Yin, Y. S. Wang, L. J. Wan, L. Gu and Y. G. Guo, *Angew. Chem., Int. Ed.*, 2016, **55**, 7445–7449.
39 C. Zhao, Z. Yao, Q. Wang, H. Li, J. Wang, M. Liu, S. Ganapathy, Y. Lu, J. Cabana, B. Li, X. Bai, A. Aspuru-Guzik, M. Wagemaker, L. Chen and Y. S. Hu, *J. Am. Chem. Soc.*, 2020, **142**, 5742–5750.
40 J. U. Choi, J. Kim, J.-Y. Hwang, J. H. Jo, Y.-K. Sun and S.-T. Myung, *Nano Energy*, 2019, **61**, 284–294.
41 Y. Hironaka, K. Kubota and S. Komaba, *Chem. Commun.*, 2017, **53**, 3693–3696.
42 Z. Xiao, J. Meng, Q. Li, X. Wang, M. Huang, Z. Liu, C. Han and L. Mai, *Sci. Bull.*, 2018, **63**, 46–53.
43 Y. Sun, S. Guo and H. Zhou, *Energy Environ. Sci.*, 2019, **12**, 825–840.